Ultrafine MoS$_2$ Nanosheets Vertically Patterned on Graphene for High-Efficient Li-Ion and Na-Ion Storage

Chunguang Wei[1], Zhidong Hou[2], Huanhuan Sun[2] and Jian-Gan Wang[2]*

[1]Shenzhen Cubic-Science Co., Ltd., Shenzhen, China, [2]Center for Nano Energy Materials, State Key Laboratory of Solidification Processing, School of Materials Science and Engineering, Northwestern Polytechnical University, Xi'an, China

Hierarchically two-dimensional (2D) heteroarchitecture with ultrafine MoS$_2$ nanosheets vertically patterned on graphene is developed by using a facile solvothermal method. It is revealed that the strong interfacial interaction between acidic Mo precursors and graphene oxides allows for uniform and tight alignment of edge-oriented MoS$_2$ nanosheets on planar graphene. The unique sheet-on-sheet architecture is of grand advantage in synergistically utilizing the highly conductive graphene and the electroactive MoS$_2$, thus rendering boosted reaction kinetics and robust structural integrity for energy storage. Consequently, the heterostructured MoS$_2$@graphene exhibits impressive Li/Na-ion storage properties, including high-capacity delivery and superior rate/cycling capability. The present study will provide a positive impetus on rational design of 2D metal sulfide/graphene composites as advanced electrode materials for high-efficient alkali–metal ion storage.

Keywords: MoS$_2$, graphene, heterostructure, Li-ion batteries, Na-ion batteries

INTRODUCTION

The increasing social concern on natural resources (e.g., fossil fuels) and environmental problems (e.g., climate change) has triggered extensive research activities on the development of sustainable and renewable resources of solar energy and wind power (Yang et al., 2011). Accordingly, energy storage systems such as electrochemical energy storage (EES) devices are indispensable to promote the utilization of these intermittent energy resources (Wang et al., 2015). In particular, rechargeable battery technologies, including Li-ion batteries and Na-ion batteries, stand at the forefront of the EES devices due to their high energy density (Yabuuchi et al., 2014). To meet the ever-increasing demands of energy/power densities for applications ranging from portable consumer electronics and electric vehicles to large-scale smart utility grids, it is of great necessity to improve the battery performance by developing advanced electrode materials.

Two-dimensional (2D) nanomaterials have drawn significant attention in recent years and have shown great promise in energy storage applications (Chhowalla et al., 2013; Anasori et al., 2017). Transition metal dichalcogenides (TMDs) represent a class of promising 2D nanomaterials for use in Li-ion/Na-ion batteries (Xu et al., 2014; Yun et al., 2018; Zhu et al., 2021). Among the well-studied TMDs, MoS$_2$ has been considered to be a prominent candidate due to its high specific capacity and low cost (Wu et al., 2020). MoS$_2$ shows analogous layered structure to graphite, which is composed of stacked S-Mo-S layers through van der Waals interactions (Liu et al., 2021). The unique layered 2D

nanostructure permits easy insertion/extraction of ions along the interlayer channels, provides large surface area for energy-storage sites, and reduces the electron/ion transport distances compared with the bulk counterparts (Wang et al., 2017; Yu et al., 2017). However, the structurally stable 2H-phase of MoS_2 suffers from low electrical conductivity and large volume change during charge/discharge processes, which collectively lead to poor rate performance and short cycle lifetime. To mitigate these shortcomings, the most effective strategy is hybridizing MoS_2 nanostructures with conductive carbonaceous materials, such as graphene (Teng et al., 2016; Sun et al., 2020), carbon nanotubes (Chen et al., 2016; Wang et al., 2016), carbon nanofibers (Zhou et al., 2014; Wang et al., 2017), and carbon nanoboxes (Yu et al., 2015). The carbonaceous materials not only afford high-speed conductive pathways for improving the electrical conductivity of MoS_2, but also function as flexible substrates for alleviating volume excursion, thereby enabling fast electrochemical kinetics and robust structural stability. 2D graphene (nanosheets) is of particular interest due to its large surface area, high electrical conductivity, and strong mechanical strength (Shao et al., 2015). A great deal of research activities have been made in fabricating various MoS_2/graphene nanocomposites for high-performance Li-ion/Na-ion batteries (Geng et al., 2017; Wang et al., 2017; Pan et al., 2018; Li et al., 2019). However, the Li/Na-ion storage properties of these nanocomposites are strongly associated with their hybrid morphology. The uniform anchoring of MoS_2 nanostructures tightly on the planar graphene could facilitate fast electrode kinetics and strong structural stability (Wang et al., 2020). Nevertheless, the negatively-charged graphene oxides are prone to be difficult to have a uniform coupling with the Mo-containing anions (e.g., MoO_4^{2-} and $Mo_7O_{24}^{6-}$) due to the electrostatic repulsion albeit with the assistance of cationic surfactants (Wang et al., 2013). Moreover, it is important to point out that the lithiation/sodiation of MoS_2 starts with the intercalation of Li/Na ions into the interlayers due to the large open 2D nanochannels (Shan et al., 2016; Deng et al., 2017). That is to say, edge orientation of MoS_2 on graphene may play a significant influence on the electrochemical performance. Therefore, it is highly desired to engineer the MoS_2 nanosheets with preferential edge orientation and uniform aligning on the graphene to yield a maximum harvest of energy storage.

In this work, a rational strategy is developed for preparing a hierarchical 2D heteroarchitecture of the MoS_2@graphene nanocomposite through a facile solvothermal method. The core issue is the use of acidic Mo precursors that allow for ultrafine MoS_2 nanosheets patterned on the planar graphene surface, thus constructing a unique sheet-on-sheet nanostructure. Impressively, the unique hybrid morphology could achieve a strong synergistic effect of enlarging electrode/electrolyte interfaces, reducing ion/electron transport distances and buffering large volume change of the electrode. These electrochemical characteristics are of great advantage in enhancing the Li/Na-ion energy storage with large specific capacity, superior rate capability, and outstanding cycling durability.

MATERIALS AND METHODS

Materials Synthesis

The preparation of MoS_2/reduced graphene oxide (MoS_2@rGO) was achieved by a solvothermal treatment. In specific, graphene oxide (GO) was obtained by a modified Hummers method. Then a certain amount of GO powder (20 mg) was dispersed into ultrapure water (40 ml). Subsequently, phosphomolybdic acid hydrate (100 mg) was dissolved into the GO dispersion followed by adding L-cysteine. The resulting mixture was then loaded in an autoclave and allowed to experience a solvothermal treatment of 180°C/15 h. After filtration, water rinse, and drying, black products were obtained. The as-obtained powders were finally treated by an annealing procedure of 800°C/2 h in a tube furnace under an inert N_2 gas flow. For comparison, the Mo precursor of phosphomolybdic acid was replaced by the conventional ammonium molybdate tetrahydrate (($NH_4)_6Mo_7O_{24}\cdot4H_2O$, AMT) to prepare the control sample of MoS_2@rGO-C through the similar solvothermal/annealing technique. A pure MoS_2 sample was also synthesized by the same procedure.

Materials Characterization

X-ray diffraction (XRD) (Cu Kα radiation) and a Raman spectrometer (Renishaw inVia) were used to identify the structural properties. The elemental information was recorded by X-ray photoelectron spectrometry (XPS) on an ESCALAB 250Xi. The thermal behavior of the composites was examined by thermalgravimetric analysis (TGA, Mettler Toledo TGA/DSC 3+). A Micromeritics ASAP 2020 was employed to analyze the N_2 adsorption/desorption isotherm and the corresponding porous characteristics. Morphological and structural analysis was conducted by transmission electron microscopy (TEM, Talos F200X) and scanning electron microscopy (SEM).

Electrochemical Measurements

The Li/Na-ion storage properties of the samples were evaluated based on CR 2016 coin cells, which were packed in an argon-filled glove box. A sticky slurry was prepared by dispersing 70 wt% of MoS_2-based materials, 20 wt% of conductive carbon black, and 10 wt% of polyvinylidene fluoride in a N-methyl-2-pyrrolidinone solvent. The above slurry was spread on a copper foil, and circular discs were punched out for working electrodes. The mass loading of the active materials (MoS_2/graphene or MoS_2) is about 1.2–1.5 mg^{-2}. Coin-type cells were packed by placing the counter electrode of Li foils, a Celgard 2,400 microporous polypropylene separator, and working electrodes together. The electrolyte was 1 M $LiPF_6$ in a solvent of ethylene carbonate, dimethyl carbonate, and ethylmethyl carbonate with a volume ratio of 1:1:1. The assembly of Na-ion batteries was based on Na discs and the glass fiber filter paper as the separator. The electrolyte was 1 M $NaPF_6$ in ethylene carbonate/diethyl carbonate (1:1 by volume). A CHI 660E electrochemical workstation was used to measure the cyclic voltammetry (CV) and electrochemical impedance spectra (EIS). NEWARE battery testing channels were implemented to obtain the galvanostatic
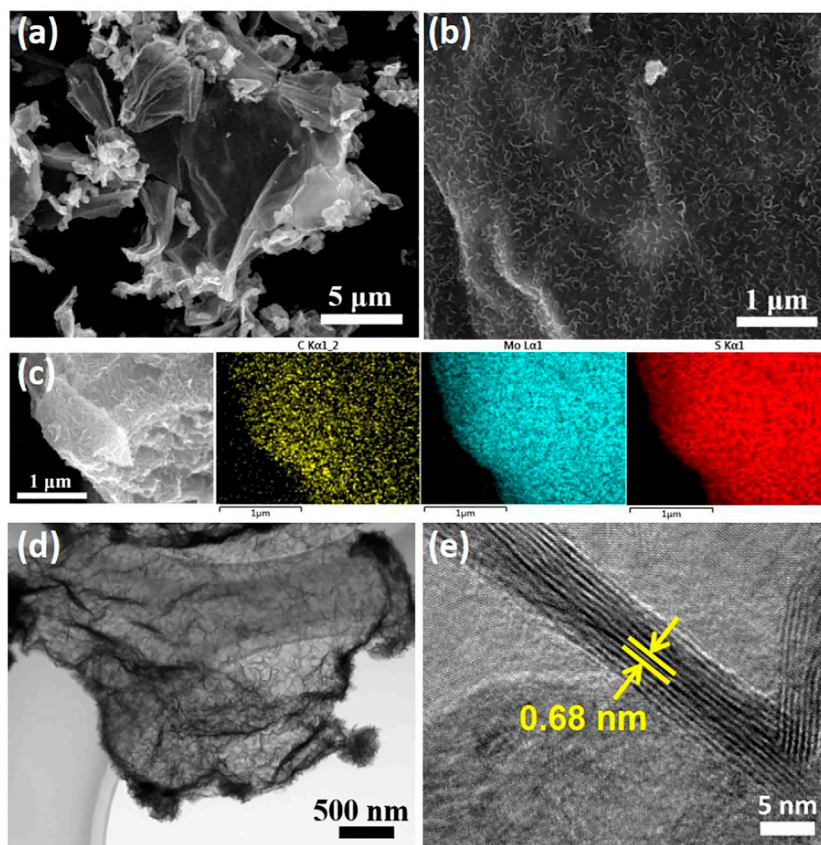
FIGURE 1 | (A,B) SEM images of the MoS$_2$@rGO composite. **(C)** EDX elemental mapping of C, Mo, and S. **(D)** TEM and **(E)** HRTEM images of MoS$_2$@rGO composite.
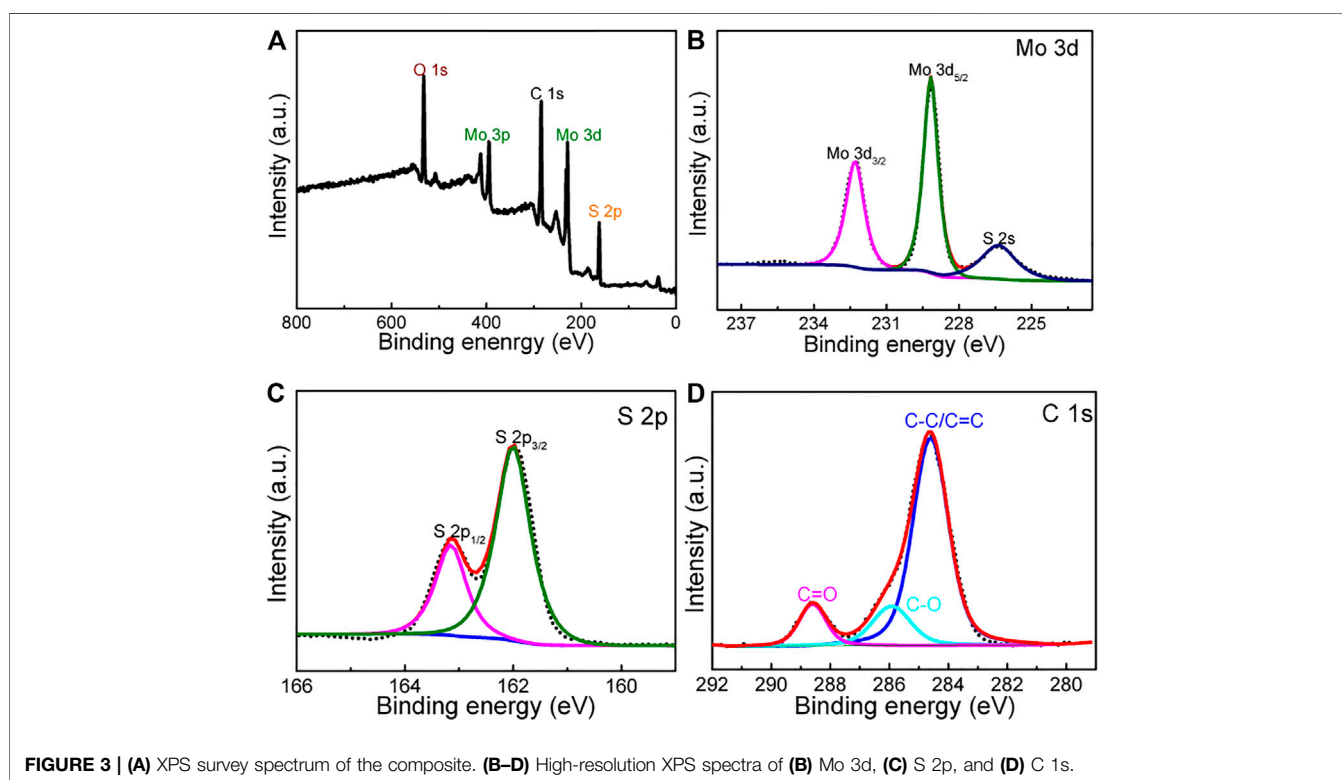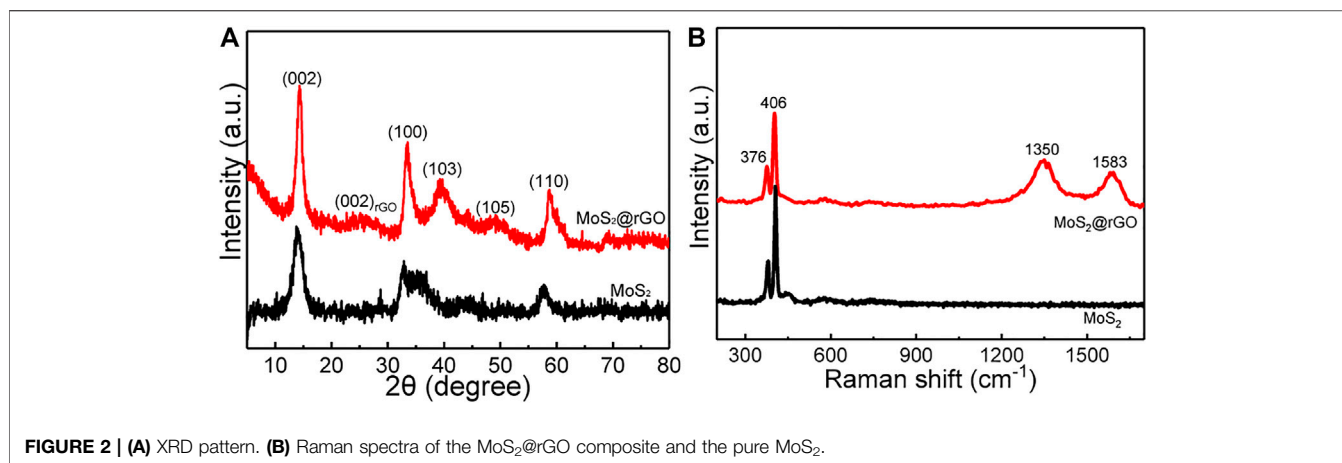
charge/discharge profiles and the cycling performance at various current rates.

RESULTS AND DISCUSSION

Figure 1A presents the panoramic SEM image of the as-prepared MoS$_2$@rGO nanocomposite. It is noticeable that the nanocomposite complies with the 2D morphology of graphene nanosheets without particle aggregation. A high-resolution snapshot (**Figure 1B**) indicates that ultrafine MoS$_2$ nanosheets are tightly and uniformly patterned on the planar graphene surface, thus building a unique 2D/2D sheet-on-sheet architecture. The homogeneous anchoring of 2D MoS$_2$ nanostructures onto the rGO nanosheets is validated by the even distribution of elemental C, Mo, and S from the energy-dispersive X-ray (EDX) mapping (**Figure 1C**). TEM imaging (**Figure 1D**) presents the hybrid sheet-on-sheet configuration, wherein the nanostructured MoS$_2$ deposits are clearly patterning on the whole rGO nanosheet surface. The associated high-resolution TEM (HRTEM) observation (**Figure 1E**) reveals vertical anchoring of ultrafine MoS$_2$ nanosheets with a thickness of 5–10 layers on the rGO. The lattice fringe spacing

of 0.68 nm corresponds well to the distance of (002) crystal facets, which surpasses the theoretical value of MoS$_2$ (0.62 nm). It is important to note that the (002)-edge-oriented and expanded MoS$_2$ nanosheets are of great benefit in boosting the electrode reaction kinetics because the electrochemical lithiation/sodiation of 2D MoS$_2$ generally occurs with an initial insertion of Li/Na ions in between the (002) interlayers.

XRD was performed to identify the crystal phase of the as-prepared samples. As shown in **Figure 2A**, the well-defined diffraction peaks with 2θ at around 14°, 33°, 39°, 49°, and 59° belong to the (002), (100), (103), (105), and (110) planes of 2H-type MoS$_2$ hexagonal phase (JCPDS # 75–1539), respectively (Kong et al., 2014). In addition, there is a broad and low-intensity peak centered at 26°, which can be ascribed to the (002) facet of the amorphous carbon structure (Wang et al., 2021). More structural information of the samples was further examined by the Raman test (**Figure 2B**). Two sharp Raman peaks are noted at 406 and 376 cm^{-1}, corresponding to the out-of-plane A$_{1g}$ and in-plane E$_{2g}^1$ bands of the 2H-MoS$_2$ phase, respectively (Xie et al., 2017). The Raman-sensitive carbon structure of rGO is clearly confirmed by the disordered carbon-related D band at 1350 cm^{-1} and the graphitic carbon-induced G band at 1583 cm^{-1}. To determine

FIGURE 2 | (A) XRD pattern. (B) Raman spectra of the MoS₂@rGO composite and the pure MoS₂.

FIGURE 3 | (A) XPS survey spectrum of the composite. (B–D) High-resolution XPS spectra of (B) Mo 3d, (C) S 2p, and (D) C 1s.

the weight ratio of MoS₂ in the composite, TGA was measured (**Supplementary Figure S1**), from which the MoS₂ component is calculated to be ~82 wt%.

XPS measurement of the MoS₂@rGO was carried out to probe the elemental composition and their bonding environment. The full-scan spectrum (**Figure 3A**) demonstrates the typical elemental signals of Mo, S, O, and C species. **Figure 2C** shows the high-resolution spectrum of Mo 3 days having two peaks locating at 232.3 (Mo3d$_{3/2}$) and 229.1 eV (Mo 3d$_{5/2}$), which agrees well with the Mo^{4+} feature of MoS₂. Moreover, the S 2p spectrum in **Figure 2D** is well resolved into two components of S 2p$_{1/2}$ (163.1 eV) and S 2p$_{3/2}$ (161.9 eV) stemming from S^{2-}

species of MoS₂. The C1s signal (**Figure 3C**) is readily fitted by three parts containing C-C/C=C (284.6 eV), C-O-C (286.2 eV), and C=O (288.5 eV) bonds. This physiochemical analysis indicates the successful production of the rGO/MoS₂ nanocomposite.

To highlight the structural advantage of the MoS₂@rGO nanocomposite, a control sample of MoS₂@rGO-C was prepared by a similar solvothermal method but using a different Mo source of ammonium molybdate ((NH₄)₆Mo₇O₂₄). The microstructure of the MoS₂@rGO-C sample is observed by SEM and TEM imaging (**Figures 4A,B**). Notably, MoS₂ nanoflowers are unevenly grown on the surface of
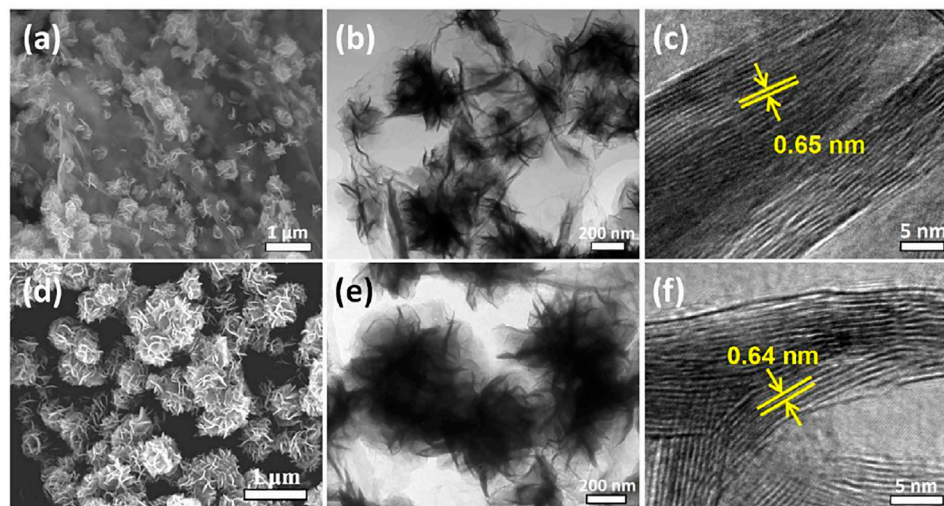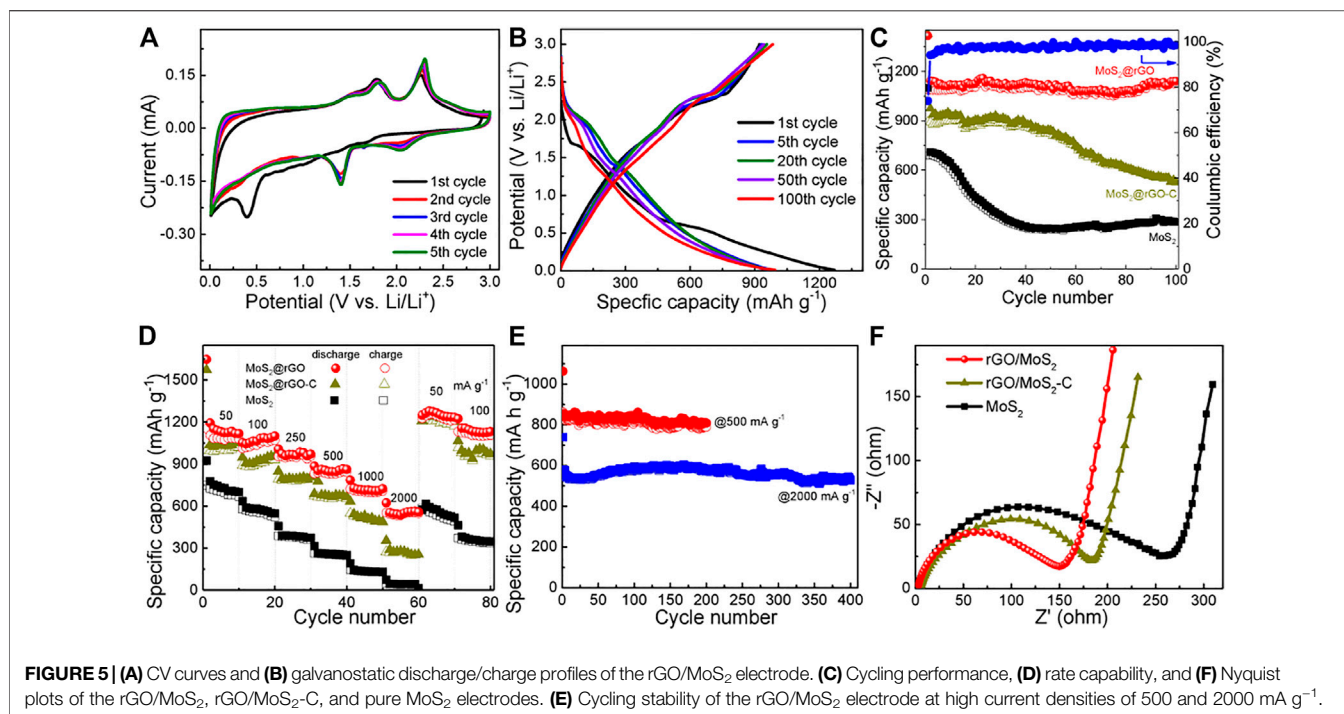
FIGURE 4 | SEM, TEM, and HRTEM images of the **(A–C)** rGO/MoS$_2$-C and **(D–F)** pure MoS$_2$.

rGO nanosheets, indicating a preferable growth behavior. The difference clearly demonstrates the great importance of the Mo source in tailoring the hybrid morphology. It is well-known that the surface of GO is negatively-charged induced by the functional species, such as carboxylic, hydroxyl, and phenolic groups, thus leading to weak chemical coupling with the Mo-containing anions because of electrostatic repulsion. The literature report established that the negatively charged GO surface can be modified toward a positively-charged state by reducing the pH value of the solution (Choi et al., 2015). In this work, the employment of phosphomolybdic acid as the Mo source significantly reduces the pH of the GO solution to <1, which potentially modifies the GO surface state for better coupling with the phosphomolybdic anions and thus enables the uniform formation of ultrafine MoS$_2$ nanosheets. As for the ammonium molybdate or sodium molybdate used in many studies, the solution pH does not change and the MoS$_2$ is prone to nucleate at some preferential sites and then grow into a large flower-like structure. For more comparison, pure MoS$_2$ submicroflowers (**Figures 4D,E**) were prepared. It is worth to mention that the petal size of the control MoS$_2$ nanosheets is much larger than that of the MoS$_2$@rGO nanocomposite, and the interlayer spacing is relatively smaller (**Figures 4C,F**).

The Li-ion storage performance of the as-prepared samples was examined. The lithiation behavior of the MoS$_2$@rGO, MoS$_2$@rGO-C and pure MoS$_2$ electrodes is first studied by the CV test at a sweep rate of 0.1 mV s^{-1}. As shown in **Figure 4A** and **Supplementary Figure S2**, the CV curves of the three electrodes are similar, indicating the identical lithiation process induced by the electroactive MoS$_2$ components (Ren et al., 2017). In specific, the broad cathodic peak at around 1.4 V in the first cycle is associated with the insertion of Li$^+$ into the interlayer space of MoS$_2$ to form Li$_x$MoS$_2$ (i.e., MoS$_2$+ xLi$^+$ + xe$^-$ → Li$_x$MoS$_2$), while the following peak at ~0.4 V corresponds to the consecutive reduction of Li$_x$MoS$_2$ to generate Li$_2$S and metallic Mo (i.e., Li$_x$MoS$_2$ + (4-x)Li$^+$ + (4-x)e$^-$ → Mo +

2Li$_2$S) and the irreversible formation of the solid-electrolyte-interface (SEI) film on the electrode surface. Upon the reverse scans, the dominant anodic peaks at about 2.3 V are reasonably attributed to the oxidation of Li$_2$S to sulfur, and the 1.9 V peak is associated with the partial oxidation of metallic Mo to MoS$_2$. From the second and ongoing cycles, two cathodic peaks are observed at around 2.0 and 1.4 V, which comply well with the reversible reduction of sulfur (S + 2Li$^+$ + 2e → 2Li$_2$S) and MoS2, respectively. It is worth to note that the CV curves are almost overlapped from the second cycle, suggesting the superb electrochemical durability and reversibility.

The cycling performance of the electrodes is examined by the galvanostatic charge–discharge test at a current density of 100 mA g^{-1}. It is evident from **Figure 4B** and **Supplementary Figure S3** that the voltage plateaus on the profiles are in good accordance with the redox couples described in the above CV analysis. The cycling comparison of the three electrodes is exhibited in **Figure 4C**. Remarkably, the MoS$_2$@rGO electrode delivers high discharge/charge capacities of 1469/1087 mA h g^{-1}, which are much higher than that of the pure MoS$_2$ electrode (1100/687 mA h g^{-1}). As for the control MoS$_2$@rGO-C electrode, high capacities of 1428/894 mA h g^{-1} is also obtained in the first cycle, indicating the effectiveness of the conductive rGO on improving the electrochemical harvest of the electroactive MoS$_2$. Moreover, in striking contrast to the MoS$_2$@rGO-C (62.6%) and pure MoS$_2$ electrode (62.5%), the MoS$_2$@rGO electrode displays a Coulombic efficiency as high as 74% in the first cycle. The initial capacity loss is primarily stemmed from the inevitable SEI film generation and some undesirable side reactions caused by the structural defects/oxygenated carbons. The Coulombic efficiency substantially rises to 95.6% for the second cycle and preserves over 99% for the subsequent cycles, suggesting excellent reversibility of the lithiation/delithiation processes. More remarkably, there is no noticeable degradation on the specific capacity for the MoS$_2$@rGO electrode, which retains at 1128 mA h g^{-1} after 100 cycles, indicating long

FIGURE 5 | (A) CV curves and **(B)** galvanostatic discharge/charge profiles of the rGO/MoS$_2$ electrode. **(C)** Cycling performance, **(D)** rate capability, and **(F)** Nyquist plots of the rGO/MoS$_2$, rGO/MoS$_2$-C, and pure MoS$_2$ electrodes. **(E)** Cycling stability of the rGO/MoS$_2$ electrode at high current densities of 500 and 2000 mA g^{-1}.
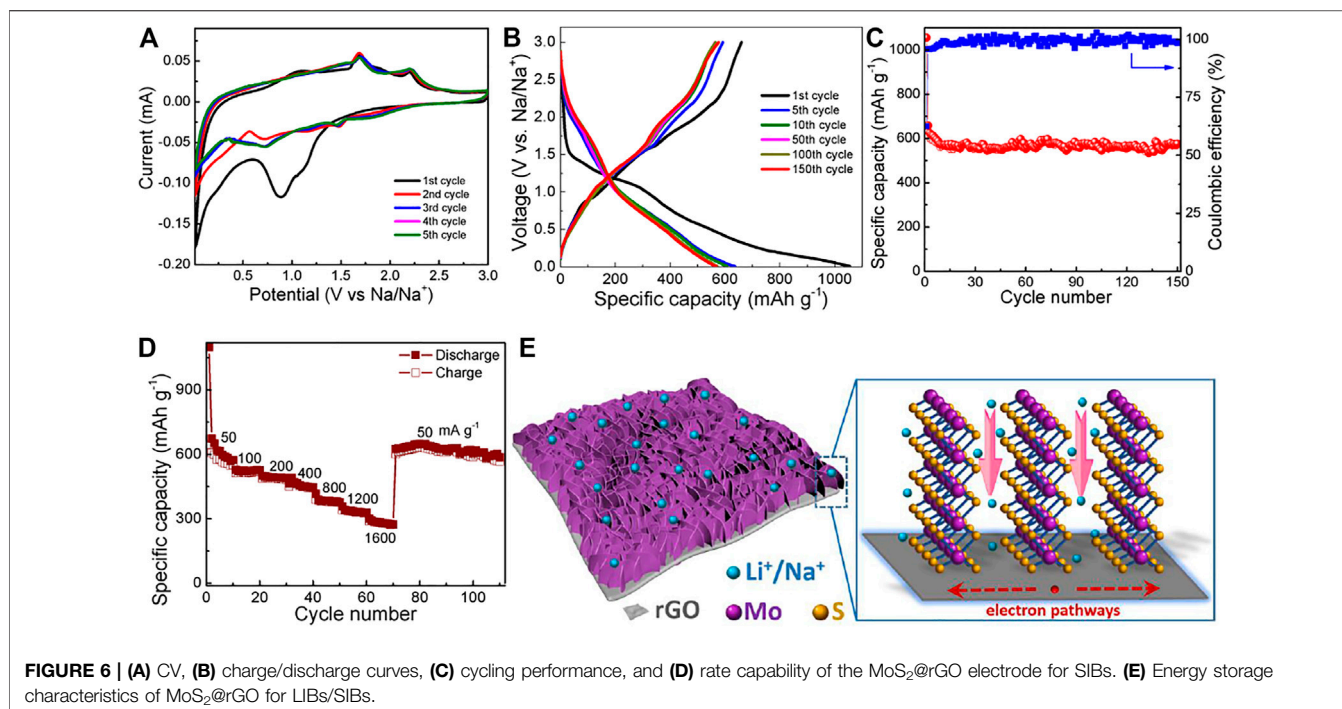
cycling lifetime. By contrast, a significant capacity decay is observed on both the MoS$_2$@rGO-C (59%) and the pure MoS$_2$ (42%) electrodes upon 100-cycling. It is noted that the capacity shows a slight increase from 70 cycles, which can be ascribed to the gradual electrode activation and the reversible formation of a gel-like film (Chen et al., 2014).

Rate capability is an important criterion for the design of high-power LIBs (Zhu et al., 2015). **Figure 4E** compares the rate capability of the MoS$_2$@rGO, MoS$_2$@rGO-C, and pure MoS$_2$ electrodes at various current densities. The hybrid rGO/MoS$_2$ is capable of delivering a Li-ion storage capacity of 1122 mA h g^{-1} at a low current rate of 50 mA g^{-1}. When the current rate elevates to 100, 250, 500, 1000, and 2000 mA g^{-1}, the reversible capacity could keep at 1037, 936, 838, 702, and 559 mA h g^{-1}, respectively. For comparison, pure MoS$_2$ is almost deprived of Li-ion storage capability at the high current rate of 2000 mA g^{-1} (43 mA h g^{-1}), while the control rGO/MoS$_2$-C electrode merely maintains at 268 mA h g^{-1} at this current rate. This comparison clearly demonstrates the superior rate performance of the rGO/MoS$_2$ electrode. Moreover, the hybrid electrode could recover the original capacity level when the current density is reduced back to 50 and 100 mA g^{-1}, again suggesting that the electrode is highly reversible and durable. The prominent cycling stability of MoS$_2$@rGO is further validated by another 2 cells tested at high current densities of 500 and 2000 mA g^{-1}. As shown in **Figure 5E**, high and stable specific capacities of 759 and 542 mA h g^{-1} are sustained after 200 cycles at 500 mA g^{-1} and 400 cycles at 2000 mA g^{-1}. Compared to the MoS$_2$@rGO-C electrode, the rGO/MoS$_2$ electrode shows substantial improvement in the cycling stability and high-rate performance. This suggests the significance of a uniform pattern and nanoscaled size of MoS$_2$ on the rGO nanosheets. It is believed that the unique heterostructure

holds great advantage on reducing the electron/ion transport pathways and maintaining the hybrid structural integrity. EIS analysis is carried out to gain an in-depth understanding of the electrode kinetics. **Figure 5F** displays the resulting Nyquist plots, in which the semicircle diameter represents the charge transfer resistance (R$_{ct}$). As expected, compared with the rGO/MoS$_2$-C (185 Ω) and pure MoS$_2$ (266 Ω) electrodes, a smaller R$_{ct}$ is noted for the rGO/MoS$_2$ electrode (151 Ω). The reduced R$_{ct}$ value implies an improved reaction kinetics, which is desirable for high power delivery.

Sodium-ion batteries (SIBs) have gained intense research activities as a promising alternative to the LIBs due to their low cost and earth-abundance of sodium in nature (Wang et al., 2018; Wu et al., 2020). Since the two battery systems share similar energy storage characteristics, it is, hence, anticipated that the unique heterostructure of MoS$_2$@rGO is also of grand benefit for Na-ion storage (Wu et al., 2021). To validate our hypothesis, the Na-ion storage properties of the MoS$_2$@rGO nanocomposites are examined. The resulting CV curves are displayed in **Figure 6A**. It is observed that the rGO/MoS$_2$ electrode exhibits very similar electrochemical behaviors in the SIBs and LIBs. The broad cathodic peak at around 1.0 V in the first cycle is associated with the insertion of Na ions into the interlayer of MoS$_2$ nanosheets and the formation of SEI layers. The sharp peak below 0.5 V in the following deep cathodic process corresponds to the conversion reaction of MoS$_2$ to form metallic Mo and Na$_2$S. The cathodic peaks in the following cycles become inconspicuous, presumably due to the gradual amorphization of crystalline MoS$_2$ after the first cycle (Wang et al., 2016). During the anodic process, the two peaks can be assigned to the consecutive oxidation of Mo

FIGURE 6 | (A) CV, **(B)** charge/discharge curves, **(C)** cycling performance, and **(D)** rate capability of the MoS$_2$@rGO electrode for SIBs. **(E)** Energy storage characteristics of MoS$_2$@rGO for LIBs/SIBs.

and Na$_2$S, respectively. In addition, the anodic peaks are almost overlapped, suggesting high reversibility and cycling stability of Na-ion storage in the hybrid electrode.

Figure 6B presents the galvanostatic charge/discharge curves of the electrode at a current density of 50 mA g^{-1}. The voltage profiles agree well with the sodiation/desodiation reactions of the CV peaks. The hybrid electrode delivers initial discharge and charge capacities of 1056 and 660 mA h g^{-1}, respectively. The huge irreversibility of the first cycle can be attributed to the formation of SEI layers and the side reactions. However, the Coulombic efficiency increases rapidly from the initial 62.5 to 95.4% (2nd cycle) and >99% in the extended cycles. **Figure 6C** exhibits the cycling performance. It is noted that the MoS$_2$@rGO electrode sustains a high capacity retention of 88% after 150 cycles, illustrating good cycling stability. Moreover, the hybrid electrode also manifests an attractive rate capability. As shown in **Figures 6A,D** a high specific capacity of 283 mA h g^{-1} is retained at a large current density of 1600 mA g^{-1}, revealing a good high-rate capability of the MoS$_2$@rGO nanocomposite for Na-ion storage. As the current density is returned back to 50 mA g^{-1}, the electrode almost recovers its initial capacity level for extended 40 cycles, confirming the long cycle life. The Na-ion storage performance of the MoS$_2$@rGO composite is compared with the previously reported MoS$_2$-based materials. As summarized in **Supplementary Table S1**, the present performance is superior or at least comparable to those documented in most studies, demonstrating the advantage of the designed MoS$_2$@rGO in SIBs.

The outstanding Li/Na-ion storage performance of the MoS$_2$@rGO electrode can be rationally ascribed to the unique hybrid morphology. **Figure 6E** schematically illustrates the energy storage characteristics of the nanocomposite for LIBs and SIBs. First, the 2D/2D nano-architecture provides sufficient surface area for

enlarging the electrode/electrolyte interfaces and thus enables more active sites for Li/Na-ion storage. Second, the nanoscaled size of the MoS$_2$ nanosheets could not only shorten the ion/electron transport distance but also minimize the volume strain caused by the lithiation/delithiation (or sodiation/desodiation) processes. Third, the preferential edge termination of MoS$_2$ facilitates fast ion transport through the open 2D nanochannels. Last but not the least, the flexible rGO network plays a role of high-speed conductive pathways for charge collection and transfer and also serves as an elastic substrate to alleviate the repetitive volume change of MoS$_2$ during cycling operation. As a result, a strong synergistic effect is achieved between the two components to rendering a high specific capacity, a superior rate capability, and long-term cycling endurance.

CONCLUSION

In summary, a hierarchical MoS$_2$@rGO heterostructure has been successfully synthesized using a facile solvothermal process. The MoS$_2$ nanosheets are uniformly and vertically patterning on the surface of graphene with preferential (002) edge orientation. The unique sheet-on-sheet nanoarchitecture could provide a sufficient number of electrochemically active sites, a reduced ion/electron transport distance, and a high-speed electrically conductive network, thereby generating a strong synergistic effect to enable enhanced electrode kinetics and high/stable electrochemical utilization of individual components. As a consequence, the MoS$_2$@rGO nanocomposite manifests a high specific capacity, superior rate, and cycling performance for use in both LIBs and SIBs. The present work demonstrates the

significance of rational engineering 2D architecture of metal sulfide/graphene to serve promising anode material candidates for high-efficient Li/Na-ion storage.

DATA AVAILABILITY STATEMENT

The original contributions presented in the study are included in the article/**Supplementary Material**; further inquiries can be directed to the corresponding author.

AUTHOR CONTRIBUTIONS

CW carried out experiments and wrote the manuscript. ZH and HS performed and analyzed experimental results. J-GW designed experiments and contributed to writing the manuscript. All authors contributed to the article and approved the submitted version.

SUPPLEMENTARY MATERIAL

The Supplementary Material for this article can be found online at: https://www.frontiersin.org/articles/10.3389/fchem.2021.802788/full#supplementary-material

REFERENCES

Anasori, B., Lukatskaya, M. R., and Gogotsi, Y. (2017). 2D Metal Carbides and Nitrides (MXenes) for Energy Storage. *Nat. Rev. Mater.* 2, 16098. doi:10.1038/natrevmats.2016.98

Chen, Y. M., Yu, X. Y., Li, Z., Paik, U., and Lou, X. W. (2016). Hierarchical MoS2 Tubular Structures Internally Wired by Carbon Nanotubes as a Highly Stable Anode Material for Lithium-Ion Batteries. *Sci. Adv.* 2, e1600021. doi:10.1126/sciadv.1600021

Chen, Y., Song, B., Tang, X., Lu, L., and Xue, J. (2014). Ultrasmall Fe3O4Nanoparticle/MoS2Nanosheet Composites with Superior Performances for Lithium Ion Batteries. *Small* 10, 1536–1543. doi:10.1002/smll.201302879

Chhowalla, M., Shin, H. S., Eda, G., Li, L.-J., Loh, K. P., and Zhang, H. (2013). The Chemistry of Two-Dimensional Layered Transition Metal Dichalcogenide Nanosheets. *Nat. Chem* 5, 263–275. doi:10.1038/nchem.1589

Choi, S. H., Ko, Y. N., Lee, J.-K., and Kang, Y. C. (2015). 3D MoS2-Graphene Microspheres Consisting of Multiple Nanospheres with Superior Sodium Ion Storage Properties. *Adv. Funct. Mater.* 25, 1780–1788. doi:10.1002/adfm.201402428

Deng, Z., Jiang, H., Hu, Y., Liu, Y., Zhang, L., Liu, H., et al. (2017). 3D Ordered Macroporous MoS₂@C Nanostructure for Flexible Li-Ion Batteries. *Adv. Mater.*, 29, 1603020. doi:10.1002/adma.201603020

Geng, X., Jiao, Y., Han, Y., Mukhopadhyay, A., Yang, L., and Zhu, H. (2017). Freestanding Metallic 1T MoS₂ with Dual Ion Diffusion Paths as High Rate Anode for Sodium-Ion Batteries. *Adv. Funct. Mater.* 27. 1702998. doi:10.1002/adfm.201770234

Kong, D., He, H., Song, Q., Wang, B., Lv, W., Yang, Q.-H., et al. (2014). Rational Design of MoS2@graphene Nanocables: towards High Performance Electrode Materials for Lithium Ion Batteries. *Energy Environ. Sci.* 7, 3320–3325. doi:10.1039/c4ee02211d

Li, Y., Zhang, R., Zhou, W., Wu, X., Zhang, H., and Zhang, J. (2019). Hierarchical MoS2 Hollow Architectures with Abundant Mo Vacancies for Efficient Sodium Storage. *ACS Nano* 13, 5533–5540. doi:10.1021/acsnano.9b00383

Liu, H., Wang, J.-G., Hua, W., You, Z., Hou, Z., Yang, J., et al. (2021). Boosting Zinc-Ion Intercalation in Hydrated MoS2 Nanosheets toward Substantially Improved Performance. *Energ. Storage Mater.* 35, 731–738. doi:10.1016/j.ensm.2020.12.010

Pan, Q., Zhang, Q., Zheng, F., Liu, Y., Li, Y., Ou, X., et al. (2018). Construction of MoS2/C Hierarchical Tubular Heterostructures for High-Performance Sodium Ion Batteries. *ACS Nano* 12, 12578–12586. doi:10.1021/acsnano.8b07172

Ren, W., Zhang, H., Guan, C., and Cheng, C. (2017). Ultrathin MoS2Nanosheets@ Metal Organic Framework-Derived N-Doped Carbon Nanowall Arrays as Sodium Ion Battery Anode with Superior Cycling Life and Rate Capability. *Adv. Funct. Mater.* 27, 1702116. doi:10.1002/adfm.201702116

Shan, T.-T., Xin, S., You, Y., Cong, H.-P., Yu, S.-H., and Manthiram, A. (2016). Combining Nitrogen-Doped Graphene Sheets and MoS2 : A Unique Film-Foam-Film Structure for Enhanced Lithium Storage. *Angew. Chem.* 128, 12975–12980. doi:10.1002/ange.201606870

Shao, Y., El-Kady, M. F., Wang, L. J., Zhang, Q., Li, Y., Wang, H., et al. (2015). Graphene-based Materials for Flexible Supercapacitors. *Chem. Soc. Rev.* 44, 3639–3665. doi:10.1039/c4cs00316k

Sun, H., Liu, H., Hou, Z., Zhou, R., Liu, X., and Wang, J.-G. (2020). Edge-terminated MoS2 Nanosheets with an Expanded Interlayer Spacing on Graphene to Boost Supercapacitive Performance. *Chem. Eng. J.* 387, 124204. doi:10.1016/j.cej.2020.124204

Sun, H., Wang, J.-G., Zhang, Y., Hua, W., Li, Y., and Liu, H. (2018). Ultrafast Lithium Energy Storage Enabled by Interfacial Construction of Interlayer-Expanded MoS2/N-Doped Carbon Nanowires. *J. Mater. Chem. A.* 6, 13419–13427. doi:10.1039/c8ta04852e

Teng, Y., Zhao, H., Zhang, Z., Li, Z., Xia, Q., Zhang, Y., et al. (2016). MoS2 Nanosheets Vertically Grown on Graphene Sheets for Lithium-Ion Battery Anodes. *ACS Nano* 10, 8526–8535. doi:10.1021/acsnano.6b03683

Wang, G., Zhang, J., Yang, S., Wang, F., Zhuang, X., Müllen, K., et al. (2018). Vertically Aligned MoS2Nanosheets Patterned on Electrochemically Exfoliated Graphene for High-Performance Lithium and Sodium Storage. *Adv. Energ. Mater.* 8, 1702254. doi:10.1002/aenm.201702254

Wang, J.-G., Kang, F., and Wei, B. (2015). Engineering of MnO2-Based Nanocomposites for High-Performance Supercapacitors. *Prog. Mater. Sci.* 74, 51–124. doi:10.1016/j.pmatsci.2015.04.003

Wang, J.-G., Ren, L., Hou, Z., and Shao, M. (2020). Flexible Reduced Graphene Oxide/prussian Blue Films for Hybrid Supercapacitors. *Chem. Eng. J.* 397, 125521. doi:10.1016/j.cej.2020.125521

Wang, J.-G., Zhou, R., Jin, D., Xie, K., and Wei, B. (2017a). Uniform Growth of MoS 2 Nanosheets on Carbon Nanofibers with Enhanced Electrochemical Utilization for Li-Ion Batteries. *Electrochimica Acta* 231, 396–402. doi:10.1016/j.electacta.2017.01.108

Wang, J., Wang, J. G., Liu, H., You, Z., Li, Z., Kang, F., et al. (2021). A Highly Flexible and Lightweight MnO 2/Graphene Membrane for Superior Zinc-Ion Batteries. *Adv. Funct. Mater.* 31, 2007397. doi:10.1002/adfm.202007397

Wang, P., Tian, J., Hu, J., Zhou, X., and Li, C. (2017b). Supernormal Conversion Anode Consisting of High-Density MoS2 Bubbles Wrapped in Thin Carbon Network by Self-Sulfuration of Polyoxometalate Complex. *ACS Nano* 11, 7390–7400. doi:10.1021/acsnano.7b03665

Wang, Y., Ma, Z., Chen, Y., Zou, M., Yousaf, M., Yang, Y., et al. (2016a). Controlled Synthesis of Core-Shell Carbon@MoS2Nanotube Sponges as High-Performance Battery Electrodes. *Adv. Mater.* 28, 10175–10181. doi:10.1002/adma.201603812

Wang, Y., Qu, Q., Li, G., Gao, T., Qian, F., Shao, J., et al. (2016b). 3D Interconnected and Multiwalled Carbon@MoS2@Carbon Hollow Nanocables as Outstanding Anodes for Na-Ion Batteries. *Small* 12, 6033–6041. doi:10.1002/smll.201602268

Wang, Z., Chen, T., Chen, W., Chang, K., Ma, L., Huang, G., et al. (2013). CTAB-assisted Synthesis of Single-Layer MoS2-Graphene Composites as Anode Materials of Li-Ion Batteries. *J. Mater. Chem. A.* 1, 2202–2210. doi:10.1039/c2ta00598k

Wu, J., Ciucci, F., and Kim, J. K. (2020a). Molybdenum Disulfide Based Nanomaterials for Rechargeable Batteries. *Chem. Eur. J.* 26, 6296–6319. doi:10.1002/chem.201905524

Wu, J., Ihsan-Ul-Haq, M., Ciucci, F., Huang, B., and Kim, J.-K. (2021). Rationally Designed Nanostructured Metal Chalcogenides for Advanced Sodium-Ion Batteries. *Energ. Storage Mater.* 34, 582–628. doi:10.1016/j.ensm.2020.10.007

Wu, J., Liu, J., Cui, J., Yao, S., Ihsan-Ul-Haq, M., Mubarak, N., et al. (2020b). Dual-phase MoS2 as a High-Performance Sodium-Ion Battery Anode. *J. Mater. Chem. A.* 8, 2114–2122. doi:10.1039/c9ta11913b

Xie, D., Xia, X., Zhong, Y., Wang, Y., Wang, D., Wang, X., et al. (2017). Exploring Advanced Sandwiched Arrays by Vertical Graphene and N-Doped Carbon for Enhanced Sodium Storage. *Adv. Energ. Mater.* 7, 1601804. doi:10.1002/aenm.201601804

Xu, X., Liu, W., Kim, Y., and Cho, J. (2014). Nanostructured Transition Metal Sulfides for Lithium Ion Batteries: Progress and Challenges. *Nano Today* 9, 604–630. doi:10.1016/j.nantod.2014.09.005

Yabuuchi, N., Kubota, K., Dahbi, M., and Komaba, S. (2014). Research Development on Sodium-Ion Batteries. *Chem. Rev.* 114, 11636–11682. doi:10.1021/cr500192f

Yang, Z., Zhang, J., Kintner-Meyer, M. C. W., Lu, X., Choi, D., Lemmon, J. P., et al. (2011). Electrochemical Energy Storage for green Grid. *Chem. Rev.* 111, 3577–3613. doi:10.1021/cr100290v

Yu, X.-Y., Hu, H., Wang, Y., Chen, H., and Lou, X. W. D. (2015). Ultrathin MoS2Nanosheets Supported on N-Doped Carbon Nanoboxes with Enhanced Lithium Storage and Electrocatalytic Properties. *Angew. Chem. Int. Ed.* 54, 7395–7398. doi:10.1002/anie.201502117

Yu, X.-Y., Yu, L., and Lou, X. W. D. (2016). Metal Sulfide Hollow Nanostructures for Electrochemical Energy Storage. *Adv. Energ. Mater.* 6, 1501333. doi:10.1002/aenm.201501333

Yun, Q., Lu, Q., Zhang, X., Tan, C., and Zhang, H. (2018). Three-Dimensional Architectures Constructed from Transition-Metal Dichalcogenide Nanomaterials for Electrochemical Energy Storage and Conversion. *Angew. Chem. Int. Ed.* 57, 626–646. doi:10.1002/anie.201706426

Zhou, F., Xin, S., Liang, H.-W., Song, L.-T., and Yu, S.-H. (2014). Carbon Nanofibers Decorated with Molybdenum Disulfide Nanosheets: Synergistic Lithium Storage and Enhanced Electrochemical Performance. *Angew. Chem. Int. Ed.* 53, 11552–11556. doi:10.1002/anie.201407103

Zhu, C., Mu, X., van Aken, P. A., Maier, J., and Yu, Y. (2015). Fast Li Storage in MoS2-Graphene-Carbon Nanotube Nanocomposites: Advantageous Functional Integration of 0D, 1D, and 2D Nanostructures. *Adv. Energ. Mater.* 5, 1401170. doi:10.1002/aenm.201401170

Zhu, L., Yang, X.-X., Xiang, Y.-H., Kong, P., and Wu, X.-W. (2021). Neurons-system-like Structured SnS2/CNTs Composite for High-Performance Sodium-Ion Battery Anode. *Rare Met.* 40, 1383–1390. doi:10.1007/s12598-020-01555-6